

Polarized radiance distribution measurements of skylight. I. System description and characterization

Kenneth J. Voss and Yi Liu

A new system to measure the natural skylight polarized radiance distribution has been developed. The system is based on a fish-eye lens, CCD camera system, and filter changer. With this system sequences of images can be combined to determine the linear polarization components of the incident light field. Calibration steps to determine the system's polarization characteristics are described. Comparisons of the radiance measurements of this system and a simple pointing radiometer were made in the field and agreed within 10% for measurements at 560 and 670 nm and 25% at 860 nm. Polarization tests were done in the laboratory. The accuracy of the intensity measurements is estimated to be 10%, while the accuracy of measurements of elements of the Mueller matrix are estimated to be 2%. © 1997 Optical Society of America

1. Introduction

The intensity and polarization of skylight have long been studied for many reasons. Early interest involved explaining natural phenomena such as the color of the sky and rainbows.^{1,2} Since the discovery of skylight polarization by Arago in 1809, studies of the polarization of skylight and neutral points have been emphasized, as these can be used as indicators of atmospheric turbidity.^{3,4}

Early measurements of skylight polarization were made mainly by visual means. As the semiconductor technology advanced, new photodetectors in conjunction with computer technology made the automatic measurements of light and its polarization possible. A large number of optical systems have been developed for observations of polarized light in various fields. Coulson¹ lists the various types of polarimeter developed for observations of the Earth's atmosphere and surface. Although photomultiplier tubes have been used as detectors for most of the systems, some devices use other detectors such as silicon cells or photographic film for special purposes. Video polarimetry techniques have also been developed that use three TV cameras for atmospheric science⁵ and CCD cameras for the natural light field.⁶ Imaging Stokes polarimetry using CCD image sen-

sors⁷ has the advantage of processing data on a pixel-by-pixel basis; thus data over a wide field of view can be obtained. The polarimeter described in this paper takes advantage of Stokes polarimetry by using a CCD image sensor and a fish-eye lens as the input optics, thus permitting measurement of Stokes parameters over the whole hemisphere.

This system is based on the RADS-II Electro-optic Fish-eye Camera Radiance Distribution System (RADS).⁸ This system uses a fish-eye camera lens, a filter changer, and a cooled CCD image sensor to measure a hemisphere of the spectral radiance distribution. With the spectral filter changer, measurement at several spectral bands can be performed in a short time (minutes). With dichroic sheet-type polarizers placed in one of the filter wheels, RADS-II becomes an analyzer-type polarimeter (RADS-IIP). With proper calibration RADS-IIP enables spectral measurement of the skylight polarized radiance distribution. The data process involves taking three data images with the polarizers in different orientations, i.e., the preferred transmission axes oriented in different directions, and these images are combined to acquire three of the light field Stokes parameters.

In this paper we discuss the overall design of the RADS-IIP system and the calibration steps unique to the polarization system, specifically the characterization of the instrument in Mueller matrix representation. Radiometric calibration of the RADS without polarization was described previously⁹ and is not discussed in detail here; only aspects specific to this system are included, and we show results of a field comparison with a simple unpolarized radiometer.

The authors are with Department of Physics, University of Miami, Coral Gables, Florida 33124-8046.

Received 16 December 1996.

0003-6935/97/246083-12\$10.00/0

© 1997 Optical Society of America

Spectral polarization radiance distribution measurements at different sites, aerosol optical thickness, and Sun angles will be presented in a future paper.¹⁰

2. Background Information

It is useful to define the radiometric quantities that we will need. The radiance is defined as the amount of radiant power d^2P_λ at wavelength λ within a wavelength interval $d\lambda$ and a differential solid angle $d\Omega$, which crosses an element of area dA and in the direction making an angle θ to the normal of dA :

$$L_\lambda(\theta, \phi) = \frac{d^2P_\lambda(\theta, \phi)}{\cos \theta \, dA \, d\Omega \, d\lambda}. \quad (1)$$

Implicit in the radiance is the directional dependence of the quantity. The collection of radiance information for all angles is the radiance distribution. The commonly measured quantities of upwelling and downwelling irradiance (E_u and E_d , respectively) are simply defined as the cosine-weighted integrals of the radiance distribution over the relevant solid angles.

To describe the polarized radiance distribution, we must have a way to represent the polarization of the radiance in a given direction. A convenient representation is provided by the Stokes vector. The electric field vector \mathbf{E} of the light field can be decomposed into two components, E_l and E_r , which represent the magnitude and the phase of the electric field vectors parallel (\mathbf{l}) and perpendicular (\mathbf{r}) to a reference plane:

$$\mathbf{E} = E_l \mathbf{l} + E_r \mathbf{r}. \quad (2)$$

The reference plane is normally defined as the plane containing the incident and scattered beams in scattering problems. Assuming that a coherent electromagnetic wave propagates in the z direction ($\mathbf{r} \times \mathbf{l}$) with a frequency ω and that amplitudes and phases for the electric fields of an electromagnetic wave in the \mathbf{l} and the \mathbf{r} directions are a_l , a_r , and δ_l , δ_r , respectively, then

$$E_l = a_l \cos(kz - \omega t + \delta_l), \quad E_r = a_r \cos(kz - \omega t + \delta_r), \quad (3)$$

where $k = 2\pi/\lambda$ is the wave constant. In general the tip of the electric vector described in Eqs. (2) and (3) forms an ellipse. To describe the elliptically polarized wave, three independent parameters, such as those of the Stokes vector¹¹ (first introduced by Stokes¹² in 1852), are needed,

$$\begin{aligned} I &= E_l E_l^* + E_r E_r^*, \\ Q &= E_l E_l^* - E_r E_r^*, \\ U &= E_l E_r^* + E_r E_l^*, \\ V &= -i(E_l E_r^* - E_r E_l^*). \end{aligned} \quad (4)$$

For a coherent wave, I , Q , U , and V are real quantities that satisfy the following equation:

$$I^2 = Q^2 + U^2 + V^2. \quad (5)$$

Assume the ellipse has a major axis (length b) and a minor axis (length c) and that the major axis makes an angle χ with the \mathbf{l} direction. The four Stokes parameters can also be expressed in terms of I , χ , and β ($\tan \beta = c/b$) by direct analyses as

$$\begin{aligned} I &= I_l + I_r, \\ Q &= I_l - I_r = I \cos 2\beta \cos 2\chi, \\ U &= I \cos 2\beta \sin 2\chi, \\ V &= I \sin 2\beta. \end{aligned} \quad (6)$$

In representing the wave by using Eqs. (4) or (6), we have assumed a constant amplitude and phase. However, the actual light field consists of many simple waves in very rapid succession. As a result, measurable intensities are associated with the superposition of many millions of simple waves with independent phases. In this case it is straightforward to prove that

$$I^2 \geq Q^2 + U^2 + V^2. \quad (7)$$

The degree of polarization, P_+ , and the degree of linear polarization, $P(\text{linear})$, are useful parameters and can be defined as

$$P_+ = (Q^2 + U^2 + V^2)^{1/2}/I \quad (8)$$

$$P(\text{linear}) = (Q^2 + U^2)^{1/2}/I. \quad (9)$$

The plane of polarization and the ellipticity are defined as

$$\tan 2\chi = U/Q, \quad (10)$$

$$\sin 2\beta = V/(Q^2 + U^2 + V^2)^{1/2}. \quad (11)$$

For partially polarized light the Stokes parameters (I , Q , U , V) can be decomposed into two vectors, a completely unpolarized component and elliptically polarized component, as

$$\begin{bmatrix} I \\ Q \\ U \\ V \end{bmatrix} = \begin{bmatrix} (Q^2 + U^2 + V^2)^{1/2} \\ Q \\ U \\ V \end{bmatrix} + \begin{bmatrix} I - (Q^2 + U^2 + V^2)^{1/2} \\ 0 \\ 0 \\ 0 \end{bmatrix}. \quad (12)$$

Transformation of a Stokes vector (I_o , Q_o , U_o , V_o) into a new Stokes vector (I , Q , U , V) by an optical process (scattering, optical elements, reflection, refraction, etc.) can be represented as a linear process with the Mueller matrix:

$$\begin{bmatrix} I \\ Q \\ U \\ V \end{bmatrix} = \begin{bmatrix} M_{11} & M_{12} & M_{13} & M_{14} \\ M_{21} & M_{22} & M_{23} & M_{24} \\ M_{31} & M_{32} & M_{33} & M_{34} \\ M_{41} & M_{42} & M_{43} & M_{44} \end{bmatrix} \begin{bmatrix} I_o \\ Q_o \\ U_o \\ V_o \end{bmatrix}. \quad (13)$$

Consider an optical instrument with elements such as birefringent crystals, sheet polarizers, quarter-wave plates, imaging lenses, and filters. In general this instrument may cause absorption, scattering, re-

flection, and refraction, and these actions will be represented by the system's Mueller matrix. If a polarization-insensitive detector (such as a CCD array with the light at approximately normal incidence) is placed behind the optical system, then only the intensity (I) of the light exiting the system is measured. In general this intensity is due to the system's Mueller matrix and the Stokes vector of light incident on the system. If the system Mueller matrix is known and variable, it is possible that combinations of measurements may be used to measure the Stokes vector of the incoming light field. For example, when a linear polarizer is used as the optical element, its Mueller matrix can be represented as follows:

$$M_p = \begin{bmatrix} k_1 + k_2 & (k_1 - k_2)\cos 2\psi & (k_1 - k_2)\sin 2\psi & 0 \\ (k_1 - k_2)\cos 2\psi & (k_1 + k_2)\cos^2 2\psi + 2\sqrt{k_1 k_2} \sin^2 2\psi & (k_1 + k_2 - 2\sqrt{k_1 k_2})\cos 2\psi \sin 2\psi & 0 \\ (k_1 - k_2)\sin 2\psi & (k_1 + k_2 - 2\sqrt{k_1 k_2})\cos 2\psi \sin 2\psi & (k_1 + k_2)\sin^2 2\psi + 2\sqrt{k_1 k_2} \cos^2 2\psi & 0 \\ 0 & 0 & 0 & 2\sqrt{k_1 k_2} \end{bmatrix}, \quad (14)$$

where k_1 and k_2 are the transmittances of the polarizer along the preferred axis and an axis 90° to this axis. ψ is the angle between the polarizer-preferred transmittance plane and a reference plane. If a sequence of perfect polarizers ($k_1 = 1$ and $k_2 = 0$) with $\psi = 0^\circ, 45^\circ, 90^\circ$ are used as analyzers of an incoming Stokes vector (I_o, Q_o, U_o, V_o), then the resulting intensities measured by a detector after the polarizers would be

$$\begin{aligned} I_1 &= I_o + Q_o & (\psi = 0^\circ), \\ I_2 &= I_o + U_o & (\psi = 45^\circ) \\ I_3 &= I_o - Q_o & (\psi = 90^\circ). \end{aligned} \quad (15)$$

When these measurements are combined, three elements of the incoming Stokes vector I_o, Q_o , and U_o can be determined. If the circular polarization element V_o is required, then an additional step using a circular polarizer as an analyzer is needed. In general, however, light in the atmosphere is not circularly polarized, so we will not measure this quantity. In the ocean, owing to the existence of the water-air surface, light may undergo total reflection at the surface and return back to the ocean; this process will introduce a small amount of circularly polarized light.¹³

These equations form the basis of analyzer polarimeters such as the RADS-IIP. What must be determined through the calibration process are the instrumental Mueller matrix elements with each orientation of the internal polarizers. This calibration process is discussed in Section 3.

3. Instrument Description

The development of the electro-optic RADS has permitted rapid and accurate measurement of the spectral radiance distribution.^{8,14} A block diagram of this system is given in Fig. 1.

The central features of RADS-II are fish-eye optics

that allows the radiance distribution over a whole hemisphere (of spatial directions) to be imaged on the two-dimensional image sensor through the imaging optical system, a remotely controlled filter changer assembly that allows the spectral measurement region to be changed rapidly, and, in the case of RADS-IIP, a polarization filter wheel that allows the Mueller matrix of the instrument to be varied. The integration time of the CCD sensor is determined by an electromechanical shutter, which is controlled by a computer interface card. Typical image integration times are between 0.5 and 15 s; thus measurement takes place rapidly. The acquired image is digitized with a 16-bit analog-to-digital converter, and the digital images are stored in a hard drive in

the associated IBM PC computer.

The CCD camera system uses a solid-state Star-Scape II CCD camera from First Magnitude Corporation,¹⁵ which adopts the TC215 image sensor from Texas Instruments. The TC215 is a full-frame CCD image sensor that provides high-resolution image acquisition for image-processing applications. The image format measures 12 mm horizontally by 12 mm vertically. The image area contains 1018 active lines with 1000 active pixels per line. Six additional dark reference lines give a total of 1024 lines in the image area, and 24 additional dark reference pixels per line give a total of 1024 pixels per horizontal line. The digitizer adds 32 more dummy lines and 32 more dummy elements for each line; thus the actual size of a digital image is 1056×1056 pixels. The image-acquiring software provides binning features, and in all our images the data were binned into 2×2 pixel samples, resulting in a 528×528 format; thus the effective pixel size is approximately $24 \mu\text{m} \times 24 \mu\text{m}$.

A series of lens relay optics transfers the bundle of light rays from the fish-eye converter lens, through the spectral and polarization filters, and then forms an image on the CCD array. The final image size is 10.66 mm in diameter for a maximum full-angle field of view of 178° , which guarantees that the image is well within the $12 \text{ mm} \times 12 \text{ mm}$ CCD array. The maximum deviation of light rays from the instrument optical axis, at the position of the spectral interference filters, is 12° . This angular dispersion of the light rays is taken into account in the spectral calibration of the instrument system.

A. Dark Noise Analysis

In the CCD sensor, dark noise (signal with no light flux incident) of the whole camera system can be

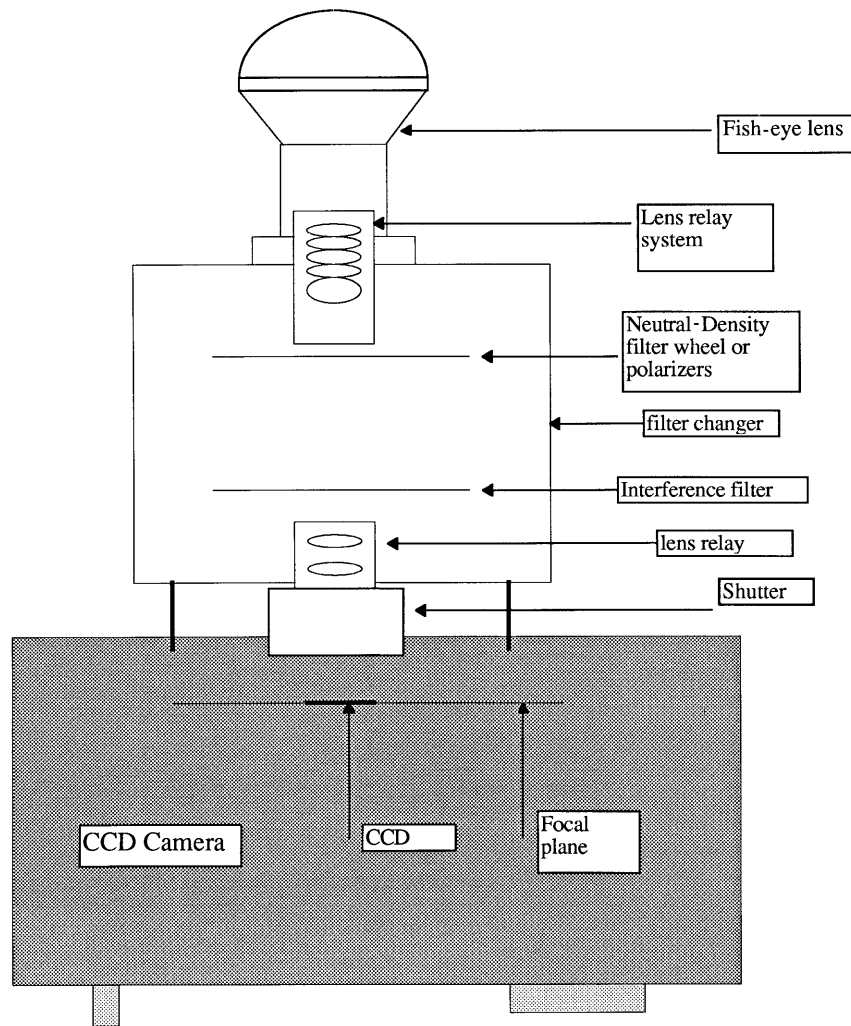


Fig. 1. Block diagram of the RADS-IIP instrument.

generated by three processes: (a) thermal generation of electrons inside the sensor array, which depends on sensor temperature and is by nature random; (b) readout noise, which depends on readout circuitry; and (c) signal-processing noise, which depends on the signal-processing (analog-to-digital converter) circuitry. In normal operation the thermoelectrically cooled TC215 image sensor temperature ranges from -30° to -40° to reduce the thermal generation of electrons.

Dark images were obtained with the shutter kept closed while the CCD was integrating. Figure 2 shows the typical dark count pattern along a row and column of the same image. Inactive and dummy pixels on the edges of the image manifest themselves in both graphs on the left and right sides. As shown, the dark current in an image is far from uniform. Figure 3 is the variation in the average dark current of a central area of 10×10 pixels on the image as a function of time and sensor temperature. This shows that the dark current increases linearly as we increase the integration time and increases exponentially as we increase the sensor temperature, as is expected.¹⁶ In

all experiments dark images were measured immediately after data images, keeping the same integration time and temperature. These dark images are subtracted from the data images during data processing.

Careful investigation of a series of dark images shows that there is also random noise after the subtraction. To reduce this random noise a series of dark images were taken under the same conditions. Images were then added, and the standard deviation of the whole image was calculated as each image was added. Application of a 3×3 averaging filter to the subtracted image is sufficient to maximize the reduction of this random noise.

B. Cross-talk Effect

Pixel cross talk can be defined as the interaction between the individual detector elements of an array detector. Blooming is a particular form of spatial cross talk that affects most array detectors. This phenomenon arises when a pixel or a localized group of pixels is overexposed to light. Blooming has appeared while the TC215 imager was used and manifests itself as spilling of charge from saturated pixels

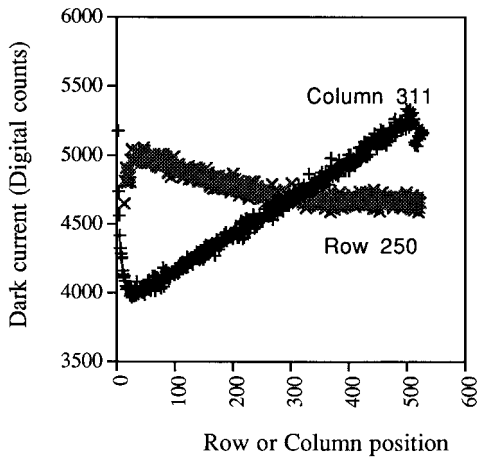


Fig. 2. Dark counts along a row and column, illustrating the nonuniformity of the dark signal on the detector. Integration time was 1 s; sensor temperature was -34.5°C .

into neighboring unsaturated pixels on the same column. Thus the information content of neighboring pixels is destroyed. This effect can limit the accuracy and dynamic range of the sensor and is avoided by adjusting the neutral-density filter or the exposure time to prevent saturation. In the sky radiance distribution measurements an occulter has been adopted to block the direct solar radiation in all field experiments to avoid this effect and to avoid camera lens flaring.

The row-column cross-talk phenomenon¹⁷ was also found on the TC215 image sensor. The existence of this effect requires that a correction algorithm be applied in image-processing programs in order to offset this interaction between pixels. Row-column cross talk means that the signal in a single pixel will affect another pixel on the same row. Investigations were made to gain qualitative and quantitative characterization of the phenomenon. An experiment was performed that illuminated only the

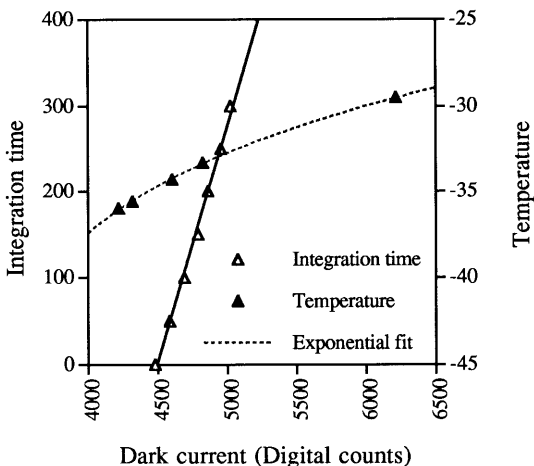


Fig. 3. Dark counts as a function of integration time and sensor temperature, illustrating the linear relation of dark counts to integration time and exponential relation to sensor temperature.

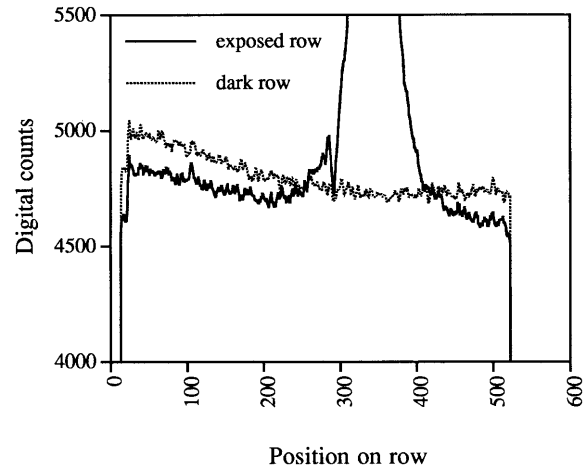


Fig. 4. Cross-talk experiment that illustrates the suppression of counts from pixels in the same row as a bright pixel.

central portion of the array. A typical result is shown in Fig. 4. In this figure, there are two curves: one curve is the signal from the pixels of the selected row after the pixels in the illuminated region were exposed to light (peak between 300 and 400), and the other curve is the same row in a corresponding dark image. While counts in the illuminated pixels increased substantially, the counts from pixels in the nonilluminated region decreased significantly with respect to dark counts. This decrease is due to the row-column cross-talk effect and is proportional to the counts in the illuminated region. A row-column cross-talk correction can be accomplished by determining the cross-talk signal for all pixels located on a given row and subtracting this from the net signal of each pixel on that same row. The cross-talk signals for all rows in an image are determined by the signals in a single column in the dark area of the data image; this single column then is duplicated to form a cross-talk signal image in which every column has the exact same information. The correction for the entire data image can be achieved by subtracting this cross-talk signal image from the data image.

C. Shutter Control

An experiment was performed to test the shutter-controlling signals and the accuracy of the exposure timing. The period of the signal opening the shutter was measured for a series of specified integration times. The result was that all input times agree with measured times within 0.2% in a range of 100 ms to 50 s. Owing to the reaction time of the shutter and the finite opening and closing times, a maximum 5-ms absolute error may still exist; thus in the field we use integration times longer than 0.5 s, which makes the maximum error from this source approximately 1%.

4. Calibration

The objective of the RADS-IIP calibration is to obtain a functional relationship between the incident flux and polarization and the instrument output. The calibration of the instrument requires a functional set of data

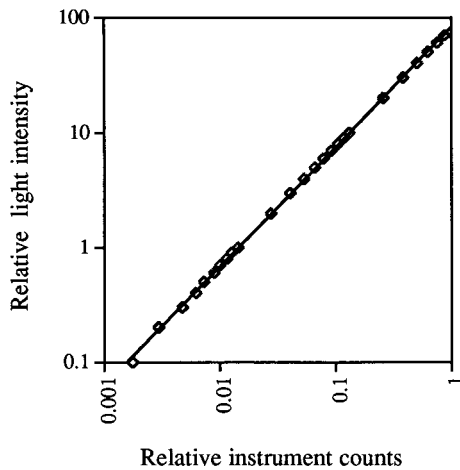


Fig. 5. Linearity calibration. Line is a power fit to the data and fits well over 3 orders of magnitude of light intensity (exponent is 1.04).

concerning the spectral, spatial, and polarization characteristics of the instrument.¹⁸ Voss and Zibordi⁹ discussed the steps required for radiometric scalar (nonpolarized) calibration of a fish-eye camera system. Calibrations of the system linearity, spectral response, camera system roll-off, and absolute system response were performed by these methods. Only the results of these steps are will be discussed.

A. Linearity and Spectral Calibration

Figure 5 shows the result of a test of the system linearity. In the experimental setup a barium sulfate reflectance plaque was illuminated in the normal direction by a stable 1000-W lamp, providing a source of stable radiance for the camera. The camera viewed the plaque at a direction 45° to the normal. The light intensity incident on the array was controlled by changing of the integration time, and an average of 3 × 3 pixels in the center of the image was obtained. This result shows that the camera output is not exactly linear but can be defined accurately over 3 orders of magnitude by a simple power function, with an exponent of 1.04.

Interference filters are used in the RADS system to select the spectral band of interest. A calibration was performed to determine the spectral response of the camera system by illuminating the system with light from a monochromator and measuring the system response. Spectral filters 1–4 were found to be centered at 439, 560, 667, and 860 nm, with full widths at half-maximum of 10.5, 10.0, 11.0, and 13.5 nm, respectively.

Figure 6 is a typical system roll-off curve determined in the calibration process; the method is described by Voss and Zibordi.⁹ This curve was found to be rotationally symmetric around the optic axis of the camera system, so the regression curve shown was used in the data reduction process. An absolute calibration of the system response was also performed with a 1000-W lamp (FEL standard lamp

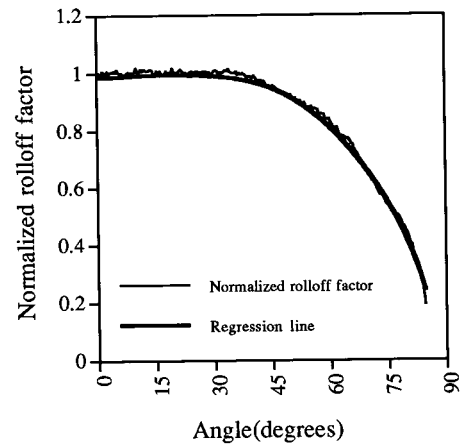


Fig. 6. Typical roll-off curve found through the calibration process.

traceable to the National Institute of Standards and Technology) and a Spectralon reflectance plaque.

B. Polarimetric Calibration

The Mueller matrix of the camera optical system can be represented as a single 4 × 4 matrix. Although in theory this Mueller matrix of the optical system can be decomposed into a chain of matrices that are representations of the individual optical components, it is better to calibrate the system as one unit using prepared sources of partially polarized light. Since the CCD array measures only intensity, only the first row of the total system Mueller matrix must be determined. In this case we input known sets of I_o , Q_o , U_o , and V_o ; I is measured; and M_{11} , M_{12} , M_{13} , and

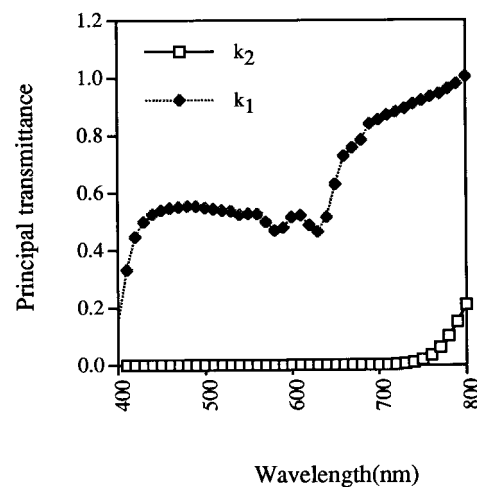


Fig. 7. Measured principal transmittances for the dichroic polarizer used as a function of wavelength.

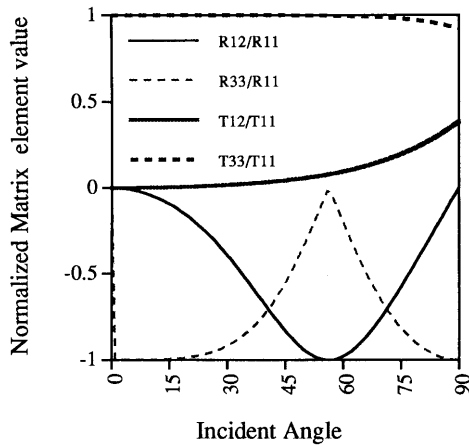


Fig. 8. Nonzero matrix elements for the reflected and transmitted light due to interaction with a glass (index of refraction of 1.5) surface.

M_{14} can be determined. A convenient set of Stokes vectors to use as input beams are¹⁹

$$A = \begin{bmatrix} I_o \\ I_o \\ 0 \\ 0 \end{bmatrix}, \quad B = \begin{bmatrix} I_o \\ -I_o \\ 0 \\ 0 \end{bmatrix}, \quad C = \begin{bmatrix} I_o \\ 0 \\ I_o \\ 0 \end{bmatrix}, \quad D = \begin{bmatrix} I_o \\ 0 \\ 0 \\ I_o \end{bmatrix}, \quad (16)$$

where A is horizontally polarized light, B is vertically polarized light, C is $+45^\circ$ polarized light, and D is right-handed circularly polarized light. These beams are sequentially input into the optical system, and the output light intensity is recorded in each case. This provides four linear equations, the solution of which determines the required elements of the system Mueller matrix.

Since we produce the linear polarization states with a dichroic sheet polarizer (Gray polarizing film, Edmund Scientific),²⁰ we need to measure the spectral polarization and transmission properties of this polarizer. The principal transmittances of the dichroic polarizers used were measured and are shown as functions of wavelength in Fig. 7. The extinction ratios, i.e., the fraction of light transmitted through a closed pair of polarizers, were found to be less than 1% for visible light. Transmission for a single dichroic polarizer acting alone ranges from 5% to 50% for visible light. Thus, using sheet polarizers and an unpolarized light source, one can generate the following light beams as input light:

$$A = \begin{bmatrix} 1 \\ \frac{k_1 - k_2}{k_1 + k_2} \\ 0 \\ 0 \end{bmatrix}, \quad B = \begin{bmatrix} 1 \\ \frac{-k_1 + k_2}{k_1 + k_2} \\ 0 \\ 0 \end{bmatrix}, \quad C = \begin{bmatrix} 1 \\ 0 \\ \frac{k_1 - k_2}{k_1 + k_2} \\ 0 \end{bmatrix}. \quad (17)$$

In general the ingoing light undergoes interactions with various optical components of the RADS. If we number each individual optical element in the order

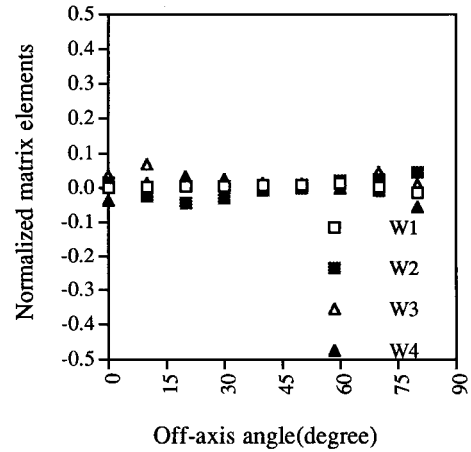


Fig. 9. Reduced matrix element M_{14} as a function of off-axis angle and polarization filter position (W1–W4).

of its presence, then the Mueller matrix can be described by the Mueller matrix of a chain of total number of optical components as follows:

$$M = \dots M_3 M_2 M_1, \quad (18)$$

where M_i is the Mueller matrix of the i th optical component. For our RADS-II system these optical components are lenses, polarizers, interference color filters, and absorption neutral-density filters. For the convenience of our analysis let us denote the Mueller matrix of the polarizer as M_p . Light interacting with the surfaces of optical components undergoes refraction for lenses, reflection and refraction for interference filters, and absorption and refraction for neutral-density filters.

The Mueller matrix for an isotropic absorption process is the unity matrix (note that all Mueller matrices below are normalized to M_{11} , and therefore we use the term reduced Mueller matrix). The reduced Mueller matrix for reflection and refraction processes

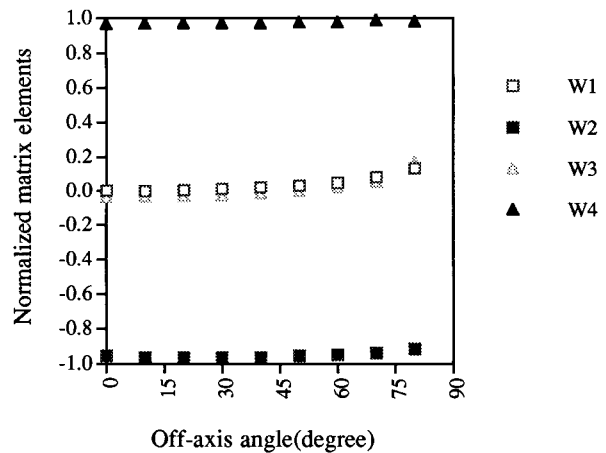


Fig. 10. Reduced matrix element M_{12} as a function of off-axis angle and polarization filter position.

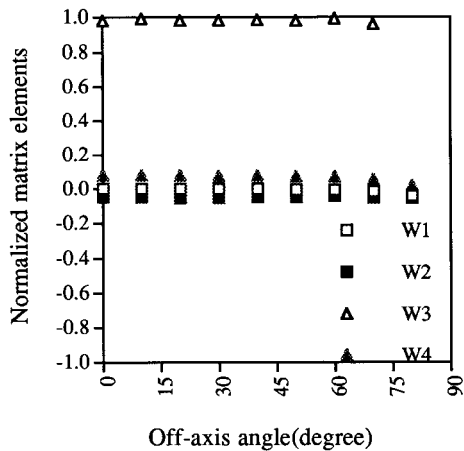


Fig. 11. Reduced matrix element M_{13} as a function of off-axis angle and polarization filter position.

has been derived by Kattawar and Adams²¹ and has the following form:

$$\begin{bmatrix} 1 & \frac{\alpha - \eta}{\alpha + \eta} & 0 & 0 \\ \frac{\alpha - \eta}{\alpha + \eta} & 1 & 0 & 0 \\ 0 & 0 & \frac{\gamma}{\alpha + \eta} & 0 \\ 0 & 0 & 0 & \frac{\gamma}{\alpha + \eta} \end{bmatrix}, \quad (19)$$

where α , η , and γ depend on incident and refracted angles. These matrix elements are plotted in Fig. 8 as a function of incident angle, assuming light entering glass (relative index of refraction 1.5).

The product of a chain of matrices with the form of Eq. (19) has the same symmetry as Eq. (19), and this allows us to write the total Mueller matrix as the product of the polarizer Mueller matrix and the Mueller matrix for all other optical components. In doing so we have made the assumption that all the contributions to the camera's Mueller matrix due to optical

components other than polarizers are from optical components before the polarizer, mainly the fish-eye input optics. This is reasonable, because only at the input stage are large refraction angles involved. Even for the interference filter every transmitted ray undergoes two refractions and pairs of reflections. The reduced Mueller matrix for double reflections at small angles is close to unity, and therefore the reduced Mueller matrix for an interference filter is nothing but double refraction at small angles, which is also close to a unity matrix. The validity of these assumptions is tested by experiment. Let M_s be the Mueller matrix due to optical components other than the polarizer, then we can write the total Mueller matrix as

$$M = M_p M_s. \quad (20)$$

Once k_1 and k_2 for polarizers are known, the Mueller matrix M_p can be calculated. Thus it is necessary only to measure the Mueller matrix for the camera without a polarizer and the orientation of the polarizer.

In the following discussions we use the notation $m_{12}(W1)$, $m_{13}(W1)$, and $m_{14}(W1)$ to denote the reduced Mueller matrix elements for the polarization filter wheel in position 1 and $m_{12}(W2)$, $m_{13}(W2)$, and $m_{14}(W2)$ for reduced Mueller matrix elements for the second position. Similar notation will be used to describe the Mueller matrix elements for the third and fourth polarizer positions. There is no polarizer in position 1, but the polarizers in positions 2, 3, and 4 are oriented at 0° , 45° , 90° , respectively, relative to an arbitrary axis.

Figure 9 shows that the measured m_{14} values for the four filter wheel locations are close to zero, as expected from the form of Eq. (19). The deviations from zero are caused by the imperfect quarter-wave plate employed in the experiment. Since we used a quarter-wave plate (at 550 nm, Melles Griot 02WRM009) made of mica, it can only approximate a quarter-wave plate at the wavelengths of the RADS-II. The Mueller matrix elements m_{12} and m_{13} are shown in Figs. 10 and 11, respectively. It can be seen that $m_{13}(W1)$ and $m_{14}(W1)$ are close to zero.

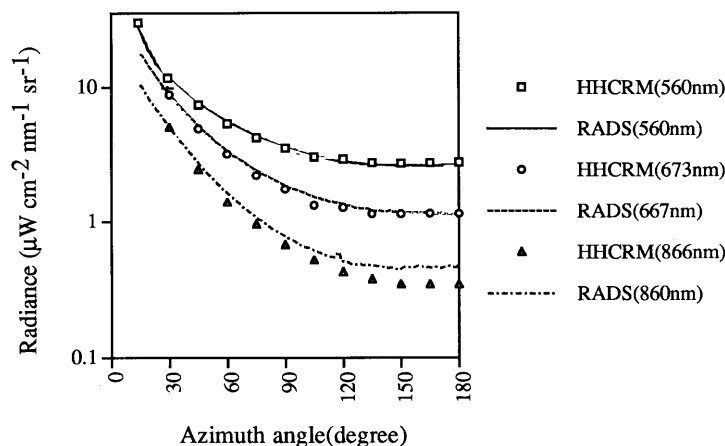


Fig. 12. Almucantar comparison of HHCRM and RADS.

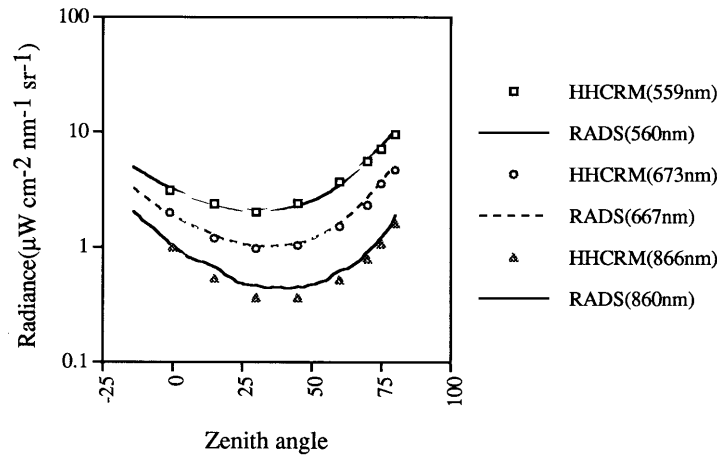


Fig. 13. Principal plane comparison of HHCRM and RADS.

These are the Mueller matrix elements of the camera without a polarizer. But $m_{12}(W1)$ is not zero and varies with incidence angle as T_{12}/T_{11} of Fig. 8. These results show that the total Mueller matrix of the camera (without polarizers) is similar to Eq. (19).

Experimentally $m_{12}(W1)$ and $m_{13}(W1)$ were found to be rotationally symmetric around the optical axis. Similar experiments were also performed to test for spectral dependence, and it was found that the Mueller matrix is independent of wavelength within experimental error. In each of these cases the system was found to be rotationally symmetric and spectrally constant within 1%.

With this method we have the following reduced Mueller matrix elements: $m_{12}(W1)$, $m_{13}(W1) = m_{14}(W1) = 0$. Applying symmetry principles to the Mueller matrix and considering that there are only reflections and refractions involved in the camera case (without a polarizer), the overall Mueller matrix has the same form as Eq. (19). Thus we can assume $m_{33}(W1) = m_{44}(W1) = 1$, $m_{23}(W1) = m_{24}(W1) = m_{34}(W1) = 0$, and the Mueller matrix for the camera [in Eq. (20)] is known. Since the Mueller matrix for a sheet polarizer is known, we are able to generate the Mueller matrix of the RADS-II for any direction of view, once the preferred transmission axis of the polarizer is known.

5. Calibration Tests

To confirm the accuracy of the scalar (nonpolarized) calibration procedures an experiment was performed in April 1994 in Key West, Florida, in conjunction with the Hand-Held Contrast Reduction Meter (HHCRM).²² Measurements of the sky radiance distribution with the RADS-II (without polarizers in place) were obtained at three wavelengths common to both instruments, 558, 673, and 866 nm. The measurement site was located at the edge of Key West, Florida.

While the RADS-II measurement was obtained quickly (typical integration time was 1 s), the HHCRM measurement had to be taken successively, one point at a time. Only principal plane and almucantar data were taken with the HHCRM. The almu-

cantar corresponds to directions with the same Sun zenith angle but varying azimuthal angles from the Sun. The principal plane is composed of directions in the plane containing the Sun and the zenith. The HHCRM measurement sequence took ~ 3 min for each wavelength. In the RADS-II measurements an occulter was used to block the direct solar radiation owing to the dynamic range limitation of the CCD sensor and to prevent flare from the direct solar beam in the camera optics. Thus no data are available within 20° of the Sun in the radiance image.

Figures 12 and 13 compare the RADS-II data with the HHCRM data for three channels at wavelengths of 560, 667, and 860 nm. It should be noted that the HHCRM has an approximate pointing inaccuracy of 2° . Figure 14 shows the relative difference of the data in the principal plane for three channels. The difference is computed as

$$\% \text{ difference} = 100 \left[\frac{\text{HHCRM} - \text{RADS}}{(\text{HHCRM} + \text{RADS})/2} \right] \quad (21)$$

The principal plane is a more difficult comparison because of pointing inaccuracies in the HHCRM and

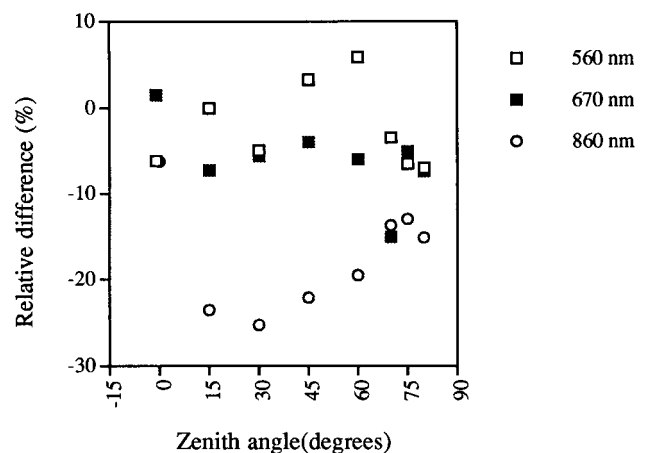


Fig. 14. Relative difference between HHCRM and RADS measurements in the principal plane at each wavelength.

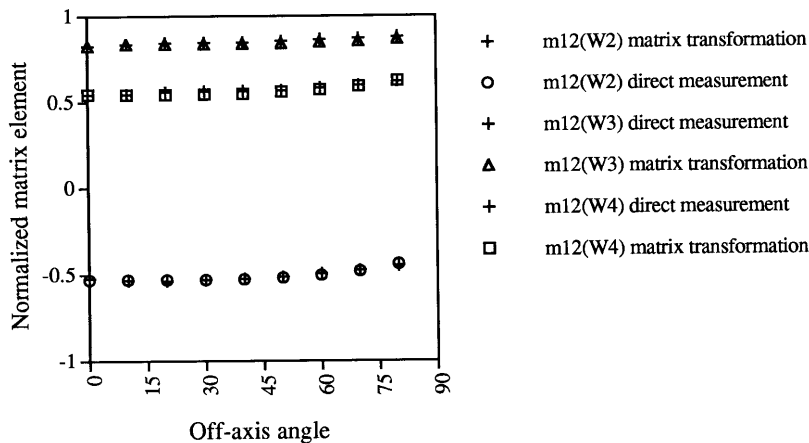


Fig. 15. *M*₁₂ direct measurement and matrix transformation method, illustrating how well the matrix transformation method works to estimate the system Mueller matrix. Measurements were performed at 560 nm.

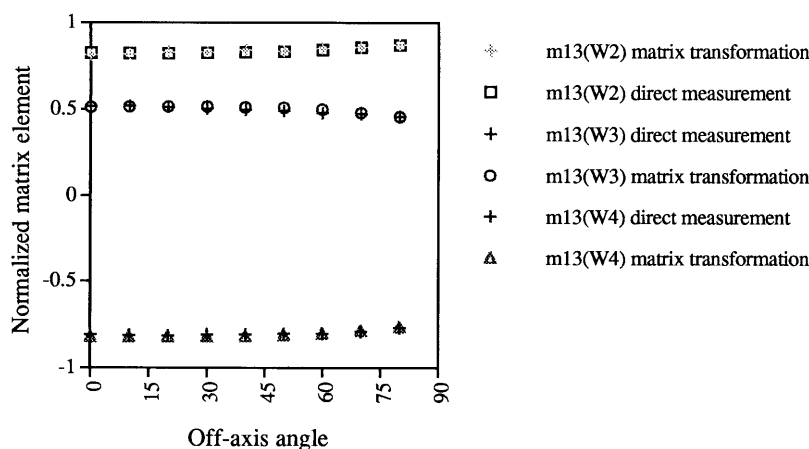


Fig. 16. *M*₁₃ direct measurement and matrix transformation method, illustrating how well the matrix transformation method works to estimate the system Mueller matrix. Measurements were performed at 560 nm.

because the roll-off calibration in the RADS enters strongly into the RADS data set.

For 560 and 670 nm all the data shown have less than a 10% difference. The agreement between RADS-II and HHCRM data for 860 nm is poor; the difference can reach as large as 25% when the radiance value is small, with RADS-II data always higher. The gain of the HHCRM is highly sensitive to temperature at this wavelength; thus the HHCRM data may not be so accurate at this wavelength.

To test the polarization calibration method (separation of polarizer and camera Mueller matrices) an experiment was performed to measure the Mueller matrix elements directly and compare them with those same elements obtained by matrix transformation [Eq. (20)]. The experimental setup is similar to the absolute calibration method in the way the camera was placed and the light source arranged. An additional device prepared light beams *A*, *B*, and *C* as in Eq. (17), and the camera viewed a reflectance plaque, illuminated by a 1000-W lamp, through this device. This device is

basically a hollow cylinder painted black, with a sheet polarizer placed on a polarizer holder in front of the cylinder. The polarizer can be precisely rotated around the cylinder's axis. The aperture of the polarizer allowed a 4° field of view. Although tests were done for all three wavelengths, Figs. 15 and 16 show the comparisons between experimental results and matrix transformation results for 560 nm. The transformed values differ from the directly measured values only by 1%–2%. The development of the matrix transformation technique for RADS-II polarimetric calibration allows the Mueller matrix elements to be computed relatively quickly for the whole hemisphere.

6. Camera System Mueller Matrix Elements for the Whole Hemisphere

So far we have illustrated the polarimetric calibration procedures for the RADS-II CCD camera system. Since the Mueller matrix elements depend on the coordinate system, it is necessary to define the coordinate system used.

Consider an *x*–*y* coordinate system on the CCD

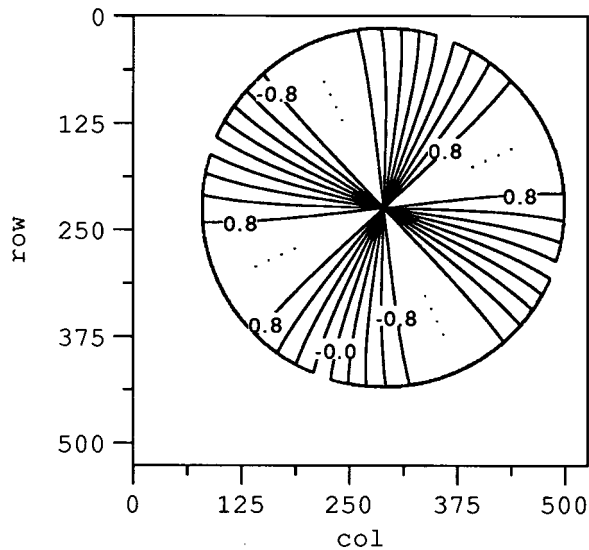


Fig. 17. Sample contour plot of $M12(W2)$.

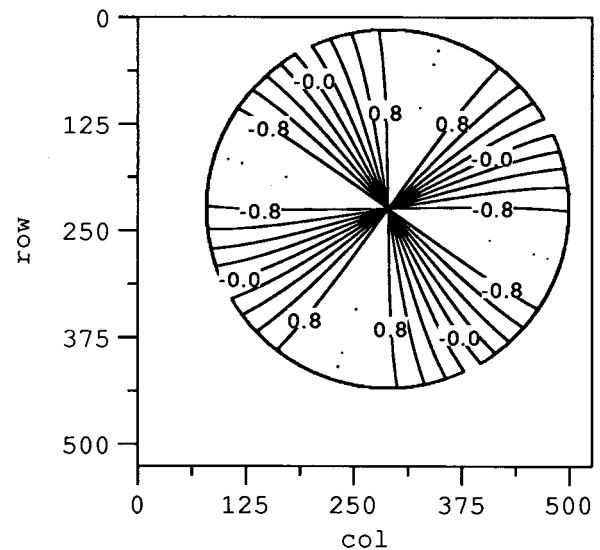


Fig. 18. Sample contour plot of $M12(W3)$.

array with z pointing normal to the array. All the Mueller matrix elements are represented in this x - y - z coordinate system for the RADS-II optical system and in describing the radiative transfer process. For the optical system of RADS-IIP each pixel on the array corresponds to a zenith and azimuth angle. The l axis of the system is in the plane defined by the specific look direction and the optic axis of the system. The zenith and azimuth angles determine the Mueller matrix elements and therefore the polarization signature of the camera system. In the previous discussions we have shown that the Mueller matrix of the camera does not depend on azimuth angle (rotationally symmetric around the optic axis). Since we know the geometric mapping of spatial direction to individual pixel on the array, it is possible to express the spatial Mueller matrix in an image format.

Figures 17–18 are example contour plots of the Mueller matrix element images for $M12$ and different configurations of polarizers, all generated from Eq. (20). The rotational symmetry is evident in these images. $M12(W1)$ varies only slowly with off-axis zenith angle. $M12(W2)$ varies strongly with zenith angle, as the incoming l axis is oriented parallel and perpendicular to the transmission axis of the polarizers' orientation shown in Fig. 17. $M12(W3)$ (shown in Fig. 18) and $M12(W4)$ are similar, except rotated at 45° azimuthally to follow the rotation of the polarizer. With these (effective) images of the Mueller matrix elements the Mueller matrix of the camera system is defined exactly. These images then provide a convenient way to store this information and operate on data acquired in the field.

7. Conclusions

We have described the RADS-IIP instrument and have shown through experiment that the system performs well. We expect that the absolute calibration of the system is accurate within 10% for most chan-

nels. Polarization measurements are accurate within approximately 2%. With the images resulting from the polarimetric calibration we can process sets of sky radiance distribution data to obtain polarized spectral radiance distributions accurately and quickly (<2 min) for all directions. Because all directions are taken simultaneously, the system is well adapted to operate in a changing environment or on a less stable platform, such as a ship. In a companion paper¹⁰ we will present data obtained with the instrument and investigate aspects of the skylight polarization.

The authors acknowledge the support of the Ocean Optics Program at the Office of Naval Research under grant N000149510309 and NASA under NAS5-31363. Also, we thank Albert Chapin for his help during the calibrations.

References

1. K. L. Coulson, *Polarization and Intensity of Light in the Atmosphere* (A. Deepak, Hampton, Va., 1988).
2. A. T. Young, "Rayleigh scattering," *Phys. Today* **35**(1), 42–48 (1982).
3. K. L. Coulson, "Characteristics of skylight at the zenith during twilight as indicators of atmospheric turbidity. I: degree of polarization," *Appl. Opt.* **19**, 3469–3480 (1980).
4. H. H. Kimball, "The effect of the atmospheric turbidity of 1912 on solar radiation intensities and skylight polarization," *Bull. Mt. Weather Obs.* **5**, 295–312 (1913).
5. T. Prosch, D. Hennings, and E. Raschke, "Video polarimetry: a new imaging technique in atmospheric science," *Appl. Opt.* **22**, 1360–1363 (1983).
6. T. W. Cronin, N. Shashar, and L. Wolff, "Portable imaging polarimeters," in *Proceedings of the Twelfth IAPR International Conference on Pattern Recognition* (Institute of Electrical and Electronics Engineers, Computer Society, Los Alamitos, Calif., 1994), pp. 606–609.
7. H. Povel, "Imaging stokes polarimetry with modulators and charge coupled-device image sensors," *Opt. Eng.* **34**, 1870–1878 (1995).
8. K. J. Voss and A. L. Chapin, "Next generation in-water radi-

- ance distribution camera system," in *Ocean Optics XI*, G. D. Gilbert, ed., Proc. SPIE **1750**, 384–387 (1992).
9. K. J. Voss and G. Zibordi, "Radiometric and geometric calibration of a visible spectral electro-optic 'fish-eye' camera radiance distribution system," *J. Atmos. Oceanic Tech.* **6**, 652–662 (1989).
 10. Y. Kiu and K. J. Voss, "Polarized radiance distribution measurement of skylight. II. Experiment and data," *Appl. Opt.* **36** (1997), to be published.
 11. H. C. van de Hulst, *Light Scattering by Small Particles* (Dover, New York, 1981).
 12. G. G. Stokes, "On the composition and resolution of streams of polarized light from different sources," *Trans. Cambridge Philos. Soc.* **9**, 233–258 (1852).
 13. G. W. Kattawar and X. Xu, "Detecting Raman scattering in the ocean by use of polarimetry," in *Ocean Optics XII*, J. S. Jaffe, ed., Proc. SPIE **2258**, 222–233 (1994).
 14. K. J. Voss, "Electro-optic camera system for measurement of the underwater radiance distribution," *Opt. Eng.* **28**, 241–247 (1989).
 15. P. J. Johnson, *Manual on Starscape II CCD Cameras* (First Magnitude Inc., Laramie, Wyo., 1992).
 16. J. S. Campbell, "TC271 characterization report," in *Area Array Image Sensor Products* (Texas Instruments, Dallas, Tex., 1994).
 17. G. R. Sims and M. B. Denton, "Spatial pixel crosstalk in a charge-injection device," *Opt. Eng.* **26**, 999–1007 (1987).
 18. C. L. Wyatt, *Radiometric Calibration: Theory and Methods* (Academic, New York, 1978).
 19. B. J. Howell, "Measurement of the polarization effects of an instrument using partially polarized light," *Appl. Opt.* **18**, 809–812 (1979).
 20. E. H. Land, "Some aspects of the development of sheet polarizers," *J. Opt. Soc. Am.* **41**, 957–963 (1951).
 21. G. W. Kattawar and C. N. Adams, "Stokes vector calculations of the submarine light field in an atmosphere-ocean with scattering according to a Rayleigh phase matrix: effect of interface refractive index on radiance and polarization," *Limnol. Oceanogr.* **34**, 1453–1472 (1989).
 22. W. H. Wilson, "Measurements of atmospheric transmittance in a maritime environment," in *Atmospheric Effects on Radiative Transfer*, C. B. Ludwig, ed., Proc. SPIE **195**, 153–159 (1979).